

Dual-wavelength quantum skyrmions from liquid crystal topological defects

Mwezi Koni,^{1,*} Fazilah Nothlawala,^{1,*} Vagharshak Hakobyan,²
Isaac Nape,¹ Etienne Brasselet,^{2,†} and Andrew Forbes^{1,‡}

¹*School of Physics, University of the Witwatersrand, Private Bag 3, Wits 2050, South Africa*

²*University of Bordeaux, CNRS, Laboratoire Ondes et Matière d'Aquitaine, Talence, France*

(Dated: July 31, 2025)

We propose a spin-orbit strategy for generating dual-wavelength quantum skyrmions, realized either as entangled photon pairs at distinct wavelengths or as heralded single-photon states at a given wavelength—regimes neither previously conceptualized nor demonstrated. By coupling a two-photon entangled state to an electrically tunable liquid crystal topological defect, we engineer both nonlocal and local skyrmionic topologies in a reconfigurable platform. These results open new directions for topological quantum state engineering and the topological richness of liquid crystals.

Skyrmions are particle-like topological objects, defined as maps between spheres and characterized by an integer Skyrme number that counts how many times the target sphere is wrapped. They have been realized in various physical systems, including atomic matter [1], chiral liquid crystals [2, 3], acoustics [4, 5], and water waves [6]. In classical optics, skyrmions are formed by combining polarization and orbital angular momentum into spin-textured fields, and have been demonstrated in evanescent waves [7], paraxial beams [8, 9], and non-paraxial light [10, 11]. Their interaction with matter reveals rich physical phenomena [12, 13], and enables robustness to noise and complex environments [14, 15]. Optical skyrmions have been generated using metasurfaces [16], graded-index lenses [17], on-chip devices [18], and spatial light modulators [19], with recent advances demonstrating topological transfer between light and matter [20, 21].

Quantum optical skyrmions were recently demonstrated both at the single-photon level [22] and in entangled photon pairs [23], opening new avenues for topological quantum optics. However, these realizations remain limited to single-wavelength configurations, with no ability to switch between entangled and single-photon topological textures within a single platform, and do not extend to heralded single-photon states. Here, we report optical skyrmions in both entangled photon pairs and heralded single photons at distinct wavelengths, using a single reconfigurable device. We demonstrate switching between these quantum topological regimes and show that the process is robust to perturbations. Finally, we unveil possible preparation of a tripartite Greenberger-Horne-Zeilinger (GHZ) entanglement, distributing quantum correlations across polarization, orbital angular momentum, and wavelength with only two photons. These results offer new routes to encode and manipulate multipartite topological entanglement in quantum optics.

Our core idea is illustrated conceptually in Fig. 1(a). We start with a dual-wavelength photon pair, entangled in both spatial (OAM) and spectral (wavelength) degrees of freedom, which then pass through a tunable, wavelength and voltage-dependent spin-orbit device. By

adjusting a control parameter p (here, an applied voltage) and applying projection schemes Π_i^x on each of the three degrees of freedom of photons $i = A, B$ with $x \in \{\text{OAM, polarization, wavelength}\}$, one can deterministically prepare (i) trivial two photon states with no topology (ii) dual-wavelength bipartite entangled skyrmion existing non-locally (shown in left panel of Fig. 1(a)) (iii) heralded single photon skyrmion (shown in right panel of Fig. 1(a)), and (iv) in principle, tripartite GHZ-like entangled states spanning polarization, OAM, and wavelength.

We now outline our scheme rigorously. Our implementation, see Fig. 1(b)(i), relies on the generation of collinear entangled pair of photons labeled A and B via type-0 non-degenerate spontaneous parametric down-conversion, pumped by a continuous-wave laser at wavelength $\lambda_0 = 532$ nm incident on a crystal with quadratic optical nonlinearity [24]. The longer- and shorter-wavelength photons satisfy energy conservation $1/\lambda_1 + 1/\lambda_2 = 1/\lambda_0$, with $\lambda_1 = 1550$ nm and $\lambda_2 = 810$ nm. Both photons emerge from the crystal with vertical polarization and are converted to right (R) or left (L) circular polarization via a broadband quarter-wave plate. Prior to any spatial or spectral filtering, assuming R polarization without loss of generality, and expressing the transverse structure in the orbital angular momentum (OAM) basis, the two-photon state—constrained by angular momentum conservation—reads

$$|\Psi\rangle = \sum_{l \in \mathbb{Z}} \sum_{k=1,2} c_{l,k} |l\rangle_A |R\rangle_A |\lambda_k\rangle_A |-l\rangle_B |R\rangle_B |\bar{\lambda}_k\rangle_B, \quad (1)$$

where $c_{l,k}$ is the joint amplitude for detecting photon A with OAM $l\hbar$ at λ_k , and photon B with OAM $-l\hbar$ at $\bar{\lambda}_k$ satisfying $1/\lambda_k + 1/\bar{\lambda}_k = 1/\lambda_0$. Spin-orbit engineering is then applied using a dual-wavelength liquid crystal q-plate [25], formed via magnetoelectric generation of a unit charge *true* liquid crystal topological defect [26], see Fig. 1(b)(ii) and Supplemental Material Sec. I for details. This yields, at each wavelength, the transformation

$$|l\rangle_i |R\rangle_i \rightarrow \sqrt{1-\eta} |l\rangle_i |R\rangle_i + \sqrt{\eta} |l-2\rangle_i |L\rangle_i, \quad (2)$$

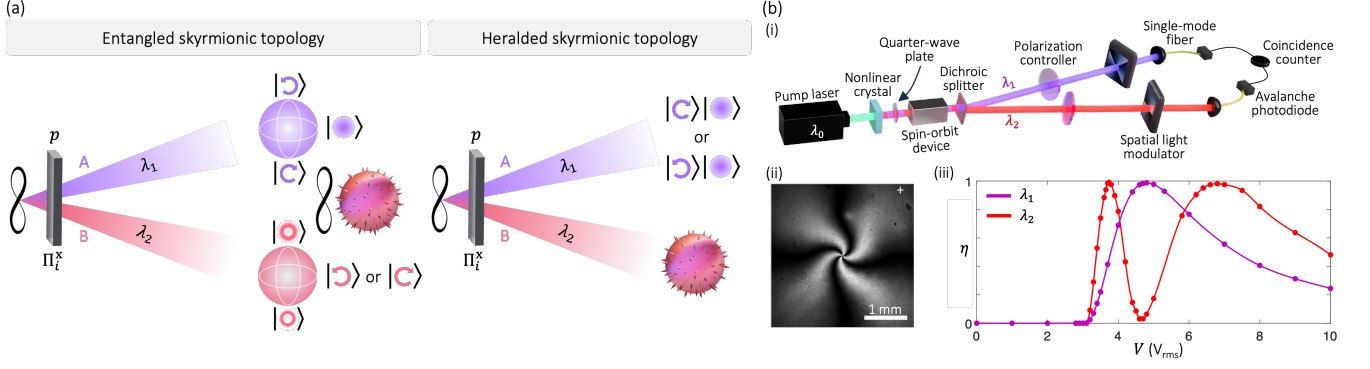


FIG. 1. (a) Illustration of the quantum topological switch. A dual-wavelength entangled photon pair described by Eq.(1) passes through a tunable, wavelength-dependent spin-orbit coupling device. By adjusting the control parameter p (in this work, an applied voltage) and applying projection schemes Π_i^x on each of the three degrees of freedom of photons $i = A, B$ with $x = (\text{OAM, polarization, wavelength})$, various quantum states can be prepared: (i) trivial two-photon states (not shown here); (ii) bipartite entangled states with nontrivial topology—either dual-wavelength nonlocal (left panel) or single-wavelength local (right panel)—corresponding to Eqs. (4)–(7); and (iii) tripartite entangled states involving polarization, orbital angular momentum, and wavelength (not shown here, see Discussion). (b)(i) Sketch of the experimental setup (see Supplemental Material Sec. II for details). (ii) Crossed linear polarizers image of the device at wavelength λ_1 and $V = 4.7 V_{rms}$. (iii) Spin-to-orbital conversion efficiency vs applied voltage.

where $i = A, B$ and η denotes the spin-to-orbital conversion efficiency of the liquid crystal device, which depends on both wavelength and applied voltage V , see Fig. 1(b)(iii).

Our approach relies on removing the spectral ambiguity from the initial entangled state $|\Psi\rangle$, without disturbing its spatial correlations. Based on this principle, we demonstrate the projection-controlled generation of distinct quantum states. This is achieved using a dichroic beam splitter that separates photons A and B into two arms, associated with wavelengths λ_1 and λ_2 , as shown in Fig. 1(b)(i). For illustration, we consider the generic case where both photons A and B undergo partial spin-to-orbital conversion, see Fig. 1(b)(iii), and, without loss of generality, set $\eta = 1/2$ to simplify the expressions. Next, photon A is coupled into a single-mode fiber, projecting it onto the $l = 0$ Gaussian mode. Although this operation acts only on photon A, it conditions the orbital state of photon B through their initial entanglement. The resulting two-photon state is

$$|\Psi'\rangle \propto (|0\rangle_B |R\rangle_B + |-2\rangle_B |L\rangle_B) |R\rangle_A + (|-2\rangle_B |R\rangle_B + |-4\rangle_B |L\rangle_B) |L\rangle_A, \quad (3)$$

which enables the generation of distinct skyrmionic quantum states from polarization measurements.

Circular polarization measurement of photon B yields two options depending on R or L choice. Namely,

$$|\Psi_{\text{nonlocal}, R}\rangle \propto |0\rangle_B |R\rangle_A + |-2\rangle_B |L\rangle_A, \quad (4)$$

$$|\Psi_{\text{nonlocal}, L}\rangle \propto |-2\rangle_B |R\rangle_A + |-4\rangle_B |L\rangle_A, \quad (5)$$

where the OAM of photon B is entangled with the polarization of photon A. These correlations define an *entangled skyrmionic topology*, with the topological structure

distributed nonlocally between spatial and polarization degrees of freedom across the two photons with distinct wavelengths defining a multi-colour skyrmion.

Alternatively, a polarization measurement on photon A in the circular polarization basis yields

$$|\Psi_{\text{local}, R}\rangle \propto |0\rangle_B |R\rangle_B + |-2\rangle_B |L\rangle_B, \quad (6)$$

$$|\Psi_{\text{local}, L}\rangle \propto |-2\rangle_B |R\rangle_B + |-4\rangle_B |L\rangle_B, \quad (7)$$

defining an *heralded skyrmionic topology* encoded locally in the polarization and spatial structure of photon B at a defined colour.

The use of single-mode fibers in both arms provides a way to manipulate the entanglement structure. Projecting photon B (rather than A) onto $l = 0$ enables (i) entanglement of photon A's OAM with photon B's polarization via polarization measurement of A, and (ii) heralding of a local skyrmionic topology onto photon A via polarization measurement of B. Moreover, tuning the spin-orbit device to zero or full spin-to-orbital conversion for photon B (A), while photon A (B) is projected onto $l = 0$, allows generation of entangled skyrmionic topologies without polarization post-selection. In contrast, applying full conversion to photon A (B) while simultaneously projecting it onto $l = 0$ suppresses entanglement, yielding a state with trivial topology.

Before probing the predicted entangled, heralded single photon, and trivial topological regimes, we verified OAM entanglement in the $l = \pm 2$ subspace by removing the spin orbit device and measuring the CHSH Bell parameter. Projective measurements onto the superposition states $|\theta_{A(B)}\rangle = \frac{1}{\sqrt{2}}(|+2\rangle + e^{i\theta_{A(B)}}|-2\rangle)$ yielded $\max(S) = 2.43$, above classical bound of 2. We fur-

ther performed a two-dimensional quantum state tomography to reconstruct the 4×4 density matrix in this subspace, obtaining fidelity $F = 0.88$, relative to the ideal Bell state, confirming the presence strong OAM entanglement. Details of the spatial-entanglement verification procedure are given in Supplementary Material, Sec. III.

Quantum state tomography becomes essential in the presence of spin-orbit coupling, where spatial and polarization degrees of freedom become entangled, as described by Eq. (2). Full spin-orbit state reconstruction is then required to access the predicted quantum topological regimes. To experimentally reveal the nonlocal and local skyrmionic topologies—respectively for dual-wavelength entangled photon pairs and heralded single photons—spin-orbit projections were performed either on both photons (nonlocal case) or on a single photon at a given wavelength (local case). Polarization projections were carried out using suitable combinations of quarter-wave plates, half-wave plates, and linear polarizers to select the standard basis states: right (R), left (L), horizontal (H), vertical (V), diagonal (D), and anti-diagonal (A). OAM projections used forked holograms displayed on spatial light modulators, as in the initial entanglement verification, but here targeting either $|-2\rangle$, $|-4\rangle$, or one of the four equal-weight superpositions $(|-2\rangle + e^{i\phi}|-4\rangle)/\sqrt{2}$ with $\phi = 0, \pi/2, \pi, 3\pi/2$. The results of these measurements are shown in Fig. 2(a), for both the dual-wavelength entangled topology and the single-wavelength heralded topologies.

This tomographic data allows determining the 4×4 spin-orbit density matrix ρ of either two-photon or single-photon states (see Supplementary Material, Sec IV, for reconstructed density matrices), from which the spatially resolved quantum Stokes vector $\mathbf{S} = (S_1, S_2, S_3)$, with norm S_0 , can be extracted [23]. In practice, we first project the full spin-orbit state ρ onto a spatial mode basis $f_n(x, y)$ of Laguerre-Gauss functions, $f_n(r) \propto (r/w)^{|l_n|} \exp(-r^2/w^2) \exp(il_n\phi)$, to obtain the reduced 2×2 polarization density matrix $\bar{\rho}(x, y) = \text{Tr}_{\text{spatial}}[\rho(P_{x,y} \otimes \mathbb{I}_{\text{pol}})]$, $P_{x,y} = |x, y\rangle\langle x, y| \otimes I_{\text{pol}}$. We then compute Stokes parameter via $S_0(x, y) = \text{Tr}[\bar{\rho}(x, y)]$, $S_k(x, y) = \text{Tr}[\bar{\rho}(x, y)\sigma_k]$, $k = 1, 2, 3$, which expresses the local Stokes vector components as projections of ρ onto the spatial position basis and the polarization Pauli operators. Expanding the density matrix in the OAM-polarization product basis, $\rho = \sum_{m,n,a,b} \tau_{mnab} |f_m, e_a\rangle\langle f_n, e_b|$, and noting $\langle x, y|f_m\rangle = f_m(x, y)$, we can express the spatially resolved Stokes components explicitly as $S_k(x, y) = \sum_{m,n,a,b} \tau_{mnab} f_m(x, y) f_n^*(x, y) \text{Tr}[\sigma_k |e_a\rangle\langle e_b|]$. The resulting maps of $\mathbf{S}(x, y)$ are shown in Fig. 2(b), with additional data provided in Sec. V of the Supplemental Material.

Each quantum Stokes vector field defines a mapping from the transverse real space to the Poincaré sphere of polarization, characterizing the local polarization expect-

tation. To quantify the topology of these polarization textures, we evaluate the Skyrme number of the normalized vector field $\mathbf{s} = \mathbf{S}/S_0$,

$$N = \frac{1}{4\pi} \iint \mathbf{s} \cdot \left(\frac{\partial \mathbf{s}}{\partial x} \times \frac{\partial \mathbf{s}}{\partial y} \right), dx, dy, \quad (8)$$

which counts how many times \mathbf{s} wraps the Poincaré sphere. We find $N \approx -2$ with less than 1% deviation in all cases, experimentally confirming the presence of second-order quantum skyrmions for both dual-wavelength entangled photon pairs and heralded single photons. Notably, had the initial two-photon state in Eq. (1) been prepared with L polarization instead of R, we would have observed oppositely charged skyrmions

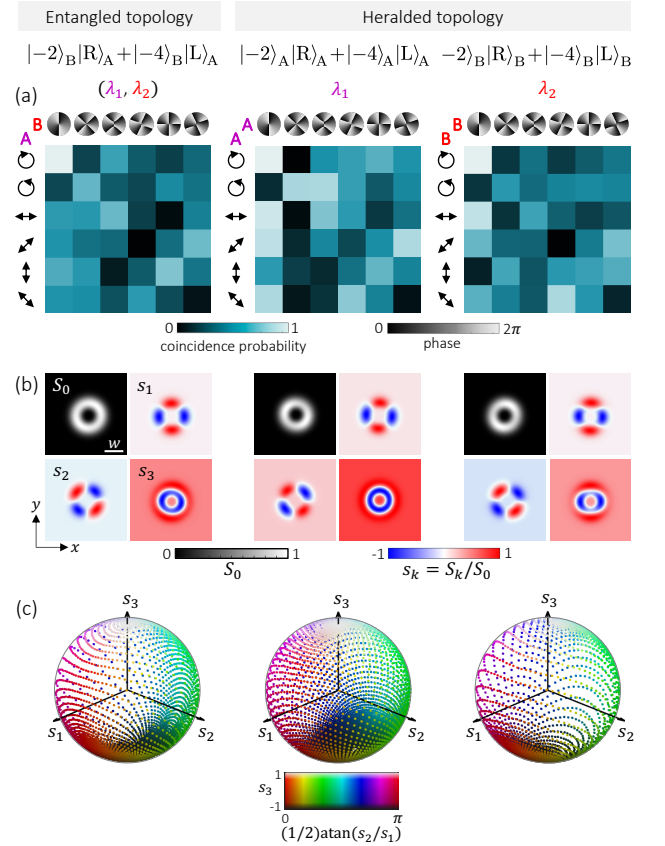


FIG. 2. Experimental observation of dual-wavelength nonlocal and single-wavelength local quantum skyrmionic topologies associated to the three main typical state under investigation. (a) Spin-orbit quantum state tomography based on combined polarization and OAM projections. Thumbnails to the left of each row indicate the polarization basis; those above each column show the spatial phase profiles of the projected state. (b) Transverse spatial distribution of the reduced Stokes vector components. (c) Corresponding Stokes vector textures mapped onto the Poincaré sphere, revealing skyrmionic polarization patterns with Skyrme number $N \simeq -2$ in all cases. Experimental parameters: $V = 3.9$ V for the entangled topology; $V = 6.3$ V and 5.4 V for the heralded topologies at λ_1 and λ_2 , respectively.

with $N = 2$.

The ability to generate entangled and heralded topologies is not limited to the specific spin-orbit configurations shown in Fig. 2, as further supported by our predictions. This is demonstrated in Fig. 3, which shows the measured Skyrme number N as a function of applied voltage for spin-orbit projections yielding either dual-wavelength two-photon states or heralded single-photon states. Notably, near $V = 4.7$ V—the voltage maximizing spin-to-orbital conversion for photon A [Fig. 1(b)(iii)] and corresponding to a trivial topology—we indeed measure $N \simeq 0$, and a typical barely covered Poincaré sphere is shown as an inset in Fig. 3. The finite voltage range over which trivial topology is observed is attributed to the low conversion efficiency for photon B, which limits detection visibility. The fidelity plot further supports this interpretation by showing the fidelity F between the reconstructed states and their ideal hybrid state counterparts. We observe that $F > 0.5$ in all regimes where $N \approx -2$, while fidelity drops below 0.5 in the trivial regime where the topology vanishes. This establishes $F > 0.5$ as an operational threshold for maintaining topological structure, and confirms the robustness of the Skyrmion configurations under voltage-induced perturbations, provided that some degree of entanglement is preserved.

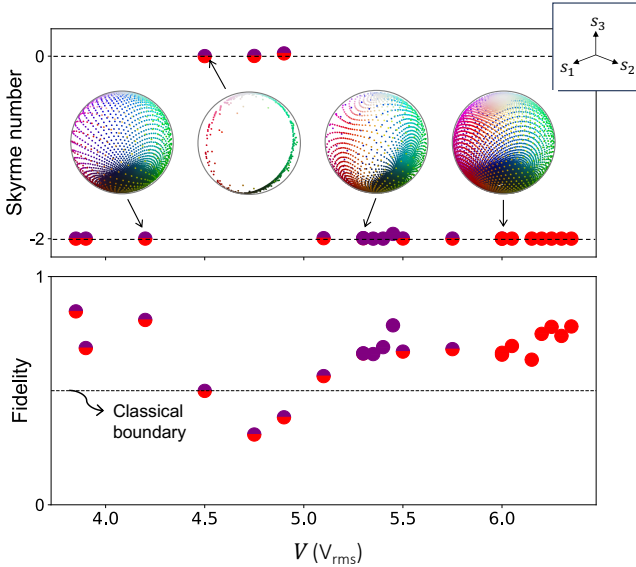


FIG. 3. Skyrme number as a function of the voltage applied to the spin-orbit device, for different circular polarization projections. Depending on the projection, the measurement probes either dual-wavelength two-photon states (bicolor markers) or heralded single-photon states (monocolor markers: purple for λ_1 , red for λ_2). Insets show typical Poincaré sphere coverage for representative cases at distinct voltage from that used in Fig. 4: dual-wavelength entangled Skyrmion ($V = 4.2$ V), dual-wavelength trivial topology ($V = 4.5$ V), and single-wavelength heralded Skyrmion ($V = 6.0$ V at λ_1 and $V = 5.3$ V at λ_2).

Finally, we illustrate our proposal for emulating a GHZ-like state across three distinct degrees of freedom, starting from the two-photon entangled state of Eq. (1), entangled in both OAM and wavelength. Assuming full spin-to-orbital conversion at λ_1 while leaving the λ_2 state unaltered—as occurs under trivial topology when spectral ambiguity is lifted by the dichroic beamsplitter—we obtain our general six particle like GHZ state (Supplementary Sec VI)

$$|\Psi\rangle = \sum_{l \in \mathbb{Z}} \gamma_l (|\lambda_1\rangle_A |L\rangle_A |l-2\rangle_A |\lambda_2\rangle_B |R\rangle_B |-l\rangle_B + |\lambda_2\rangle_A |R\rangle_A |l\rangle_A |\lambda_1\rangle_B |L\rangle_B |-l-2\rangle_B). \quad (9)$$

in which each photon encodes three logical qubits (OAM, polarization, wavelength). By projecting photon A first in spatial balanced superposition $|+l\rangle = \frac{|l\rangle + |-l-2\rangle}{\sqrt{2}}$, then in spectral balanced superposition $|+\lambda\rangle = \frac{|\lambda_1\rangle + |\lambda_2\rangle}{\sqrt{2}}$ and projecting photon B into polarization superposition $|+\sigma\rangle = \frac{|R\rangle + |L\rangle}{\sqrt{2}}$, all information about the individual eigenstates is erased, coherently selecting only two terms and heralding the three-partite state

$$|\Psi\rangle_{\text{proj}} \propto |R\rangle_A |\lambda_1\rangle_B |-l-2\rangle_B + |L\rangle_A |\lambda_2\rangle_B |-l\rangle_B. \quad (10)$$

This state exhibits genuine GHZ entanglement across photon A's polarization and photon B's OAM and wavelength, and—under the mappings $(|R\rangle_A, |L\rangle_A) \rightarrow (|0\rangle, |1\rangle)$, $(|\lambda_1\rangle_B, |\lambda_2\rangle_B) \rightarrow (|0\rangle, |1\rangle)$ and $(|-l-2\rangle_B, |-l\rangle_B) \rightarrow (|0\rangle, |1\rangle)$ is unitarily equivalent to the GHZ state $\frac{1}{\sqrt{2}}(|0, 0, 0\rangle + |1, 1, 1\rangle)$. This distinguishes our demonstration from previous works on classical and quantum optical skyrmions, where wavelength appears as an independent, separable degree of freedom, i.e., $|\Psi_{AB}\rangle = |\text{skyrmion}_{AB}\rangle \otimes |\lambda\rangle$. In contrast, here the wavelength is nonseparable and contributes intrinsically to the skyrmionic structure of the entangled wavefunction: $|\Psi_{AB}\rangle \neq |\text{skyrmion}_{AB}\rangle \otimes |\lambda\rangle$.

In conclusion, we have demonstrated projective switching between skyrmion topologies in both two-photon entangled states and heralded single-photon states—realizations so far restricted to single-wavelength configurations and not extended to heralded photons. Our dual-wavelength approach further enables voltage-controlled generation of two-photon tripartite GHZ states entangled across polarization, orbital angular momentum, and wavelength. Moreover, the scheme is robust against experimental imperfections and operates at wavelengths relevant to fiber optics and bio-imaging, hence expanding the optical skyrmion toolbox and opening new avenues for quantum technologies. From a materials standpoint, while patterned liquid crystal elements have been used in quantum optics since 2009 [27], the present work uniquely leverages true liquid crystal defects, whose topological richness—so far exploited in classical structured light [28]—now enters the quantum regime.

A. Forbes and I. Nape acknowledge funding from SA QuTI. All authors acknowledge support from the CNRS-Wits collaboration fund.

* These authors contributed equally to this work.

† etienne.brasselet@u-bordeaux.fr

‡ andrew.forbes@wits.ac.za

- [1] L. Leslie, A. Hansen, K. Wright, B. Deutsch, and N. Bigelow, *Physical Review Letters* **103**, 250401 (2009).
- [2] I. I. Smalyukh, Y. Lansac, N. A. Clark, and R. P. Trivedi, *Nature Materials* **9**, 139 (2010).
- [3] B. G.-g. Chen, P. J. Ackerman, G. P. Alexander, R. D. Kamien, and I. I. Smalyukh, *Physical review letters* **110**, 237801 (2013).
- [4] H. Ge, X.-Y. Xu, L. Liu, R. Xu, Z.-K. Lin, S.-Y. Yu, M. Bao, J.-H. Jiang, M.-H. Lu, and Y.-F. Chen, *Physical Review Letters* **127**, 144502 (2021).
- [5] R. D. Muelas-Hurtado, K. Volke-Sepúlveda, J. L. Ealo, F. Nori, M. A. Alonso, K. Y. Bliokh, and E. Brasselet, *Physical Review Letters* **129**, 204301 (2022).
- [6] B. Wang, Z. Che, C. Cheng, C. Tong, L. Shi, Y. Shen, K. Y. Bliokh, and J. Zi, *Nature* (2025), <https://doi.org/10.1038/s41586-024-08384-y>.
- [7] S. Tsesses, E. Ostrovsky, K. Cohen, B. Gjonaj, N. Lindner, and G. Bartal, *Science* **361**, 993 (2018).
- [8] R. Gutiérrez-Cuevas and E. Pisanty, *Journal of Optics* **23**, 024004 (2021).
- [9] S. Gao, F. C. Speirits, F. Castellucci, S. Franke-Arnold, S. M. Barnett, and J. B. Götte, *Physical Review A* **102**, 053513 (2020).
- [10] L. Du, A. Yang, A. V. Zayats, and X. Yuan, *Nature Physics* **15**, 650 (2019).
- [11] D. Sugic, R. Droop, E. Otte, D. Ehrmanntraut, F. Nori, J. Ruostekoski, C. Denz, and M. R. Dennis, *Nature Communications* **12**, 6785 (2021).
- [12] H. Kuratsuji and S. Tsuchida, *Physical Review A* **103**, 023514 (2021).
- [13] J. Chen, A. Forbes, and C.-W. Qiu, *Light: Science & Applications* **14**, 28 (2025).
- [14] A. A. Wang, Z. Zhao, Y. Ma, Y. Cai, R. Zhang, X. Shang, Y. Zhang, J. Qin, Z.-K. Pong, T. Marozsák, *et al.*, *Light: Science & Applications* **13**, 314 (2024).
- [15] P. Ornelas, I. Nape, R. de Mello Koch, and A. Forbes, *Nature Communications* **16**, 2934 (2025).
- [16] Y. Shen, C. He, Z. Song, B. Chen, H. He, Y. Ma, J. A. Fells, S. J. Elston, S. M. Morris, M. J. Booth, *et al.*, *Physical Review Applied* **21**, 024025 (2024).
- [17] T. He, Y. Meng, L. Wang, H. Zhong, N. Mata-Cervera, D. Li, P. Yan, Q. Liu, Y. Shen, and Q. Xiao, *Nature Communications* **15**, 10141 (2024).
- [18] W. Lin, Y. Ota, Y. Arakawa, and S. Iwamoto, *Optica* **11**, 1588 (2024).
- [19] Y. Shen, E. C. Martínez, and C. Rosales-Guzmán, *ACS Photonics* **9**, 296 (2022).
- [20] C. Mitra, C. S. Madasu, L. Gabardos, C. C. Kwong, Y. Shen, J. Ruostekoski, and D. Wilkowski, *APL Photonics* **10** (2025).
- [21] M. Lin, Q. Liu, H. Duan, L. Du, and X. Yuan, *Applied Physics Reviews* **11** (2024).
- [22] J. Liu, J. Ma, J. Yang, S. Liu, B. Chen, X. Li, C. Song, G. Qiu, K. Zou, X. Hu, *et al.*, *Nature Physics* 10.1038/s41567-025-02973-y.
- [23] P. Ornelas, I. Nape, R. de Mello Koch, and A. Forbes, *Nature Photonics* **18**, 258 (2024).
- [24] M. V. Pack, D. J. Armstrong, and A. V. Smith, *Applied Optics* **43**, 3319 (2004).
- [25] L. Yan, P. Gregg, E. Karimi, A. Rubano, L. Marrucci, R. Boyd, and S. Ramachandran, *Optica* **2**, 900 (2015).
- [26] E. Brasselet, *Physical Review Letters* **121**, 033901 (2018).
- [27] E. Nagali, F. Sciarrino, F. De Martini, L. Marrucci, B. Piccirillo, E. Karimi, and E. Santamato, *Physical Review Letters* **103**, 013601 (2009).
- [28] E. Brasselet, *Liquid Crystals: New Perspectives* (eds Pieranski P. and Godinho MH).(Hoboken: John Wiley & Sons, 2021) , 1 (2021).
- [29] J. Leach, B. Jack, J. Romero, M. Ritsch-Marte, R. Boyd, A. Jha, S. Barnett, S. Franke-Arnold, and M. Padgett, *Optics express* **17**, 8287 (2009).

SUPPLEMENTAL MATERIAL

I SPIN-ORBIT DEVICE

The spin-orbit device itself is made of a nematic liquid crystal (LC) cell and a cylindrical neodymium ring magnet. The LC cell (EHC Co. Ltd., Japan) is 10 μm thick and filled with 1859 A nematic mixture (MUT, Poland) featuring $\Delta n \simeq 0.229$ birefringence at $\lambda = 589$ nm and negative dielectric anisotropy at 100 kHz frequency. Both inner substrates are coated with indium-tin-oxide electrodes for voltage control and treated to impose homeotropic anchoring, ensuring a uniform initial molecular alignment along the optical (z) axis. The ring magnet, with a height of 6 mm, outer diameter of 8 mm, and inner diameter of 2 mm, is aligned with its axis along z and positioned approximately 2 mm above the LC layer lying in the (x, y) plane, as shown in the inset of Fig. 4 (a)(i). The combined action of the electric and magnetic fields induces the spontaneous formation of a stable topological defect with $q = +1$ charge [26]. This defect features an electrically tunable uniform birefringent phase retardation Δ and an azimuthally varying optical axis oriented at an angle $\psi = q\varphi$ relative to the x -axis, where φ is the polar angle.

II EXPERIMENTAL DETAILS

We outline experimental details of the setup shown in Fig 1 (b) (ii) of the main text to obtain our results. A collimated green diode laser of wavelength $\lambda_p = 532$ nm, and power 350 mW was sent to a temperature-controlled, Type-0 Periodically Poled Potassium Titanyl Phosphate (PPKTP) non-linear crystal of length 5 mm. The pump polarization was converted to vertical polarization and the temperature of the crystal was optimized to 60 $^\circ\text{C}$ to obtain collinear entangled photons of wavelengths, $\lambda_2 = 810$ nm and $\lambda_1 = 1550$ nm. After the crystal a quarter-wave plate (QWP) was used with the fast axis at an angle of 45° , converting the polarization from vertical to right-circular. The crystal plane was imaged onto the spin-orbit device with a beam diameter, $\omega_D = 0.7$ mm. After passing both photons through the device, a dichroic mirror was used to separate the entangled photons into two distinct arms, transmitting photons of wavelength $\lambda_2 = 810$ nm and reflecting the $\lambda_1 = 1550$ nm beam (shown as transmission in Fig. (b)(i) for simplicity). The plane of the device was imaged onto PLUTO-NIR and PLUTO-TELCO (HoloEye) spatial light modulators (SLMs) on each arm. To perform the necessary projections and state tomography, we employed two waveplates and a spatial light modulator (SLM). In the non-local case, separate projections were carried out on each arm: an SLM was used to project onto the required OAM states on one arm, while a combination of a quarter-wave

plate, half-wave plate, and linear polarizer was used on the other arm to project onto various polarization states. Due to the polarization sensitivity of SLMs, the light emerging from the SLM was horizontally polarized, allowing the SLM to function as a linear polarizer and serve as a filter for the polarization projections. The half-wave plate was rotated to access linear polarization states, and the quarter-wave plate enabled projection onto circular polarization states. In the local case, with the single-photon spin-orbit coupled state, both polarization and OAM degrees of freedom were measured locally on a single arm. After the SLMs, the photons from each arm were coupled to optical single-mode fibers (SMFs) connected to avalanche photo-diodes (APDs) for photon detection. The photon counting device (CC) measured the coincidences within a 3 ns detection window, detecting a maximum coincidence count rate of ~ 2000 counts/s.

III SPATIAL ENTANGLEMENT VERIFICATION WITHOUT SPIN-ORBIT DEVICE

Before probing the predicted nonlocal, local, and trivial topological regimes, we first verified OAM entanglement of the photon pairs generated by the nonlinear crystal. To this end, the spin-orbit device was removed and projective measurements were performed using suitable forked holograms on spatial light modulators in each arm, following the standard procedure [29]. This allowed evaluation of the Clauser-Horne-Shimony-Holt (CHSH) Bell parameter S from coincidence counts $C(\theta_A, \theta_B)$ corresponding to the joint detecting probability of photon A and B in the superposition states $|\theta_{A(B)}\rangle = \frac{1}{\sqrt{2}}(|+2\rangle + e^{i\theta_{A(B)}}|-2\rangle)$, within the OAM subspace $l = \pm 2$. Using $\theta_A \in \{0, \frac{\pi}{8}, \frac{\pi}{4}, \frac{3\pi}{8}\}$ and scanning θ_B over $[0, \pi]$, we measure $\max(S) = 2.43$ as shown in Fig. 2(a), which exceeds the classical limit $|S| = 2$ and approaches the upper quantum bound $|S| = 2\sqrt{2}$, thus confirming OAM entanglement.

The level of OAM entanglement is further assessed via quantum state tomography in this subspace, focusing on the target symmetric maximally entangled state $(|-2\rangle_A|+2\rangle_B + |+2\rangle_A|-2\rangle_B)/\sqrt{2}$. The protocol involves six projective OAM measurements per photon, defined by $|-2\rangle$, $|2\rangle$, and the four equal-weight superpositions $(|-2\rangle + e^{i\phi}|+2\rangle)/\sqrt{2}$ with $\phi = 0, \pi/2, \pi, 3\pi/2$, resulting in 36 independent coincidence counts, as shown in Fig. 2(b). We reconstruct the two-photon density matrix from these measurements by expanding in the Pauli operator basis,

$$\rho = \frac{1}{4} I_4 + \sum_{m,n=1}^3 b_{mn} \sigma_m^{(A)} \otimes \sigma_n^{(B)}, \quad (11)$$

with $\{\sigma_m\}$ the standard Pauli matrices and b_{mn} the expansion coefficients. These coefficients are obtained by

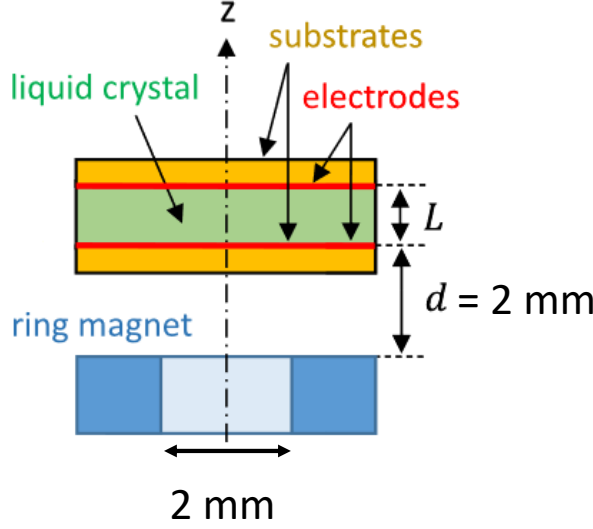


FIG. 4. **Spin-orbit device.**(a) An illustration of the schematic diagram of the device in which nematic liquid crystals are sandwiched between electrodes, and a ring magnet placed at distance $d=2$ mm. (b) Real image of packaged device highlighting the optical z axis

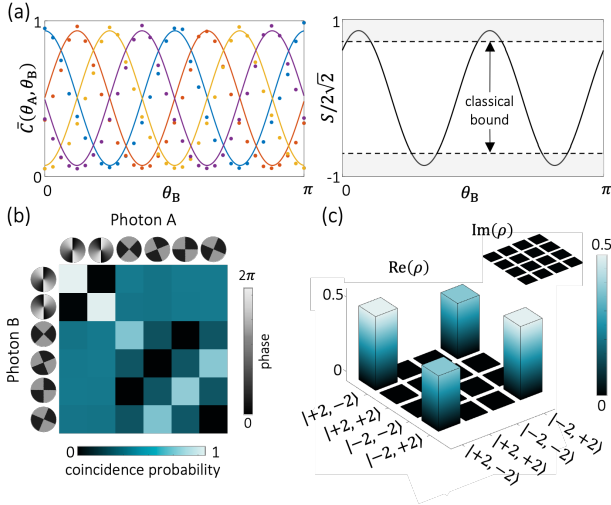


FIG. 5. Demonstration of OAM quantum entanglement of the prepared two-photon state in the absence of spin-orbit coupling. (a) Evaluation of the CHSH-Bell parameter S from joint probabilities $C(\theta_A, \theta_B)$, with $\bar{C} = \max_{\theta_A, \theta_B} C$, for $\theta_A = 0$ (blue), $\frac{\pi}{8}$ (brown), $\frac{\pi}{4}$ (orange), and $\frac{3\pi}{8}$ (purple). (b) Quantum state tomography, where the projected states of each photon are identified by thumbnails depicting the corresponding spatial phase profiles. (c) Computed real and imaginary components of the density matrix from the data shown in panel (b).

minimizing the least-squares cost function

$$\chi^2 = \sum_{i,j} [p_{ij} - \text{Tr}\{M_{ij} \rho\}]^2 \quad (12)$$

subject to $\rho \geq 0$ and $\text{Tr}\{\rho\} = 1$. The reconstructed 4×4 density matrix ρ provides full characterization of the generated quantum state, see Fig. 2(c), and the fidelity $0 \leq F \leq 1$, quantifying its similarity to the target state associated with density matrix ρ_t , yields $F = [\text{Tr}(\sqrt{\sqrt{\rho_t} \rho \sqrt{\rho_t}})]^2 = 0.88$ and confirms a high degree of entanglement.

IV SPIN-ORBIT DENSITY MATRICES

To reconstruct the spin-orbit density matrices utilized in the main text to extract spatially varying stokes parameters, we performed hybrid two-photon quantum state tomography. In the entangled regime, photon A ($\lambda_1 = 1550$ nm) is projected on to six polarization eigenstates $\{R, L, H, D, V, A\}$, while photon B ($\lambda_2 = 810$ nm) is measured in six spatial-OAM basis defined by $\{|-2\rangle, |-4\rangle\}$ and their coherent superpositions $\frac{1}{\sqrt{2}}(|-2\rangle \pm e^{i\phi} |-4\rangle)$, with $\phi = 0, \frac{\pi}{2}, \pi, \frac{3\pi}{2}$. Altogether this yields $6 \times 6 = 36$ joint projectors $M_{ij} = P_i^{(A)} \otimes P_j^{(B)}$, where $P_i^{(A)}$ and $P_j^{(B)}$ act on photon A's polarization and photon B's spatial subspaces, respectively. For each projector we record the coincidence counts C_{ij} (3 ns window) and normalize to probabilities $p_{ij} = \frac{C_{ij}}{\sum_{i,j} C_{ij}}$. In the heralded single photon regime (we imprint the topology on either on A or B), one photon is first heralded in the $|L\rangle$ polarization state; an identical 6×6 tomography is then performed on its partner, again yielding normalized probabilities p_{ij} . From these measurement we reconstruct our density matrices shown Fig 3 using the scheme outline by eqn 2

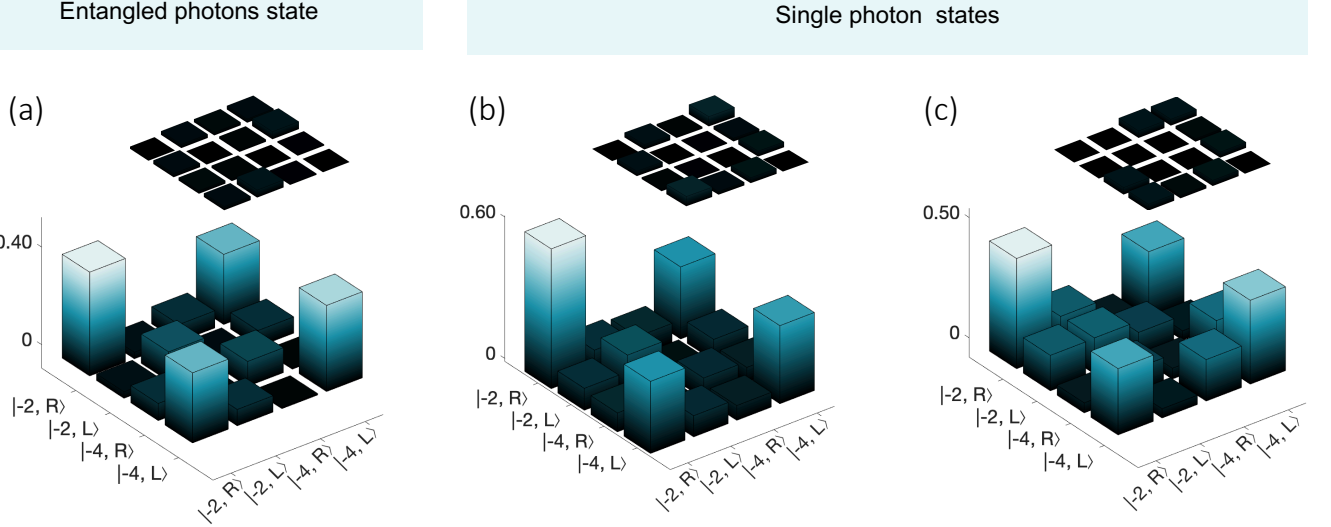


FIG. 6. **Reconstructed spin-orbit density matrices**(a) The real and imaginary parts of reconstructed density matrices for all three cases as 4×4 bar plots

V ADDITIONAL POINCARÉ SPHERE MAPPINGS

To complement the Skyrme number analysis presented in the main text, we show here the evolution of the reconstructed polarization fields $\mathbf{S}(x, y)$ projected onto the Poincaré sphere at various sampled voltage points. Each sphere shows the spatially sampled Stokes vectors mapped to the Poincaré sphere, illustrating how the extracted polarization coverage changes with applied voltage— the control parameter of spin-orbit device. As seen, broad and dense coverage of the Poincaré sphere corresponds to the topological regimes ($N \approx -2$), whereas limited coverage and polarization collapse signal the trivial regime ($N \approx 0$).

VI GHZ-LIKE STATE DERIVATION

To illustrate our proposal for emulating GHZ-like entangled states across multiple degrees of freedom (DoFs), we begin with a two-photon state entangled in both orbital angular momentum (OAM) and wavelength:

$$\sum_{l,\lambda} c_{l,\lambda} |l\rangle_A |\lambda_1\rangle_A |-l\rangle_B |\lambda_2\rangle_B |R\rangle_A |R\rangle_B. \quad (13)$$

Here, photons A and B are initially in right-circular polarization R and share entanglement in OAM $\pm l$ and wavelength (λ_1, λ_2) . We restrict ourselves to a two dimensional subspace in both OAM and wavelength, rewriting our state as

$$|\Psi\rangle = \frac{1}{\sqrt{2}} \left(|l\rangle_A |\lambda_1\rangle_A |-l\rangle_B |\lambda_2\rangle_B |R\rangle_A |R\rangle_B + |-l\rangle_B |\lambda_1\rangle_B |l\rangle_A |\lambda_2\rangle_A |R\rangle_B |R\rangle_A \right). \quad (14)$$

Next, we transform this state by applying a spin-orbit transformation plate that operates in a wavelength-selective manner. Specifically, for photons at wavelength λ_1 , the plate induces the transformation $|R, l\rangle \rightarrow |L, l-2\rangle$, while leaving photons at λ_2 unaffected. Under this transformation, the state becomes:

$$|\Psi\rangle = \frac{1}{\sqrt{2}} \left(|\lambda_1\rangle_A |L\rangle_A |l-2\rangle_A |\lambda_2\rangle_B |R\rangle_B |-l\rangle_B + |\lambda_2\rangle_A |R\rangle_A |l\rangle_A |\lambda_1\rangle_B |L\rangle_B |-l-2\rangle_B \right). \quad (15)$$

Interestingly, at this operational point, the wavelength ambiguity—normally filtered out by dichroic elements—serves as a resource, enabling superposition of orthogonal spin components. The resulting state exhibits a structure analogous to a Greenberger–Horne–Zeilinger (GHZ) state, not across three particles, but across three degrees of freedom in each of two photons: wavelength, polarization, and OAM. We make this explicit by assigning logical qubits $|0\rangle_\lambda \rightarrow |\lambda_1\rangle$, $|1\rangle_\lambda \rightarrow |\lambda_2\rangle$, $|0\rangle_\sigma \rightarrow |R\rangle$, $|1\rangle_\sigma \rightarrow |L\rangle$, $|0\rangle_l \rightarrow |l\rangle$ and $|1\rangle_l \rightarrow |l-2\rangle$. Expressed in this computational basis, the entangled state takes the form:

$$|\Psi\rangle \propto |0, 1, 1\rangle_A |1, 0, 0\rangle_B + |1, 0, 0\rangle_A |0, 1, 1\rangle_B \quad (16)$$

where each triplet denotes the qubit state for (λ, σ, l) of photon A or B. While not a canonical GHZ state,

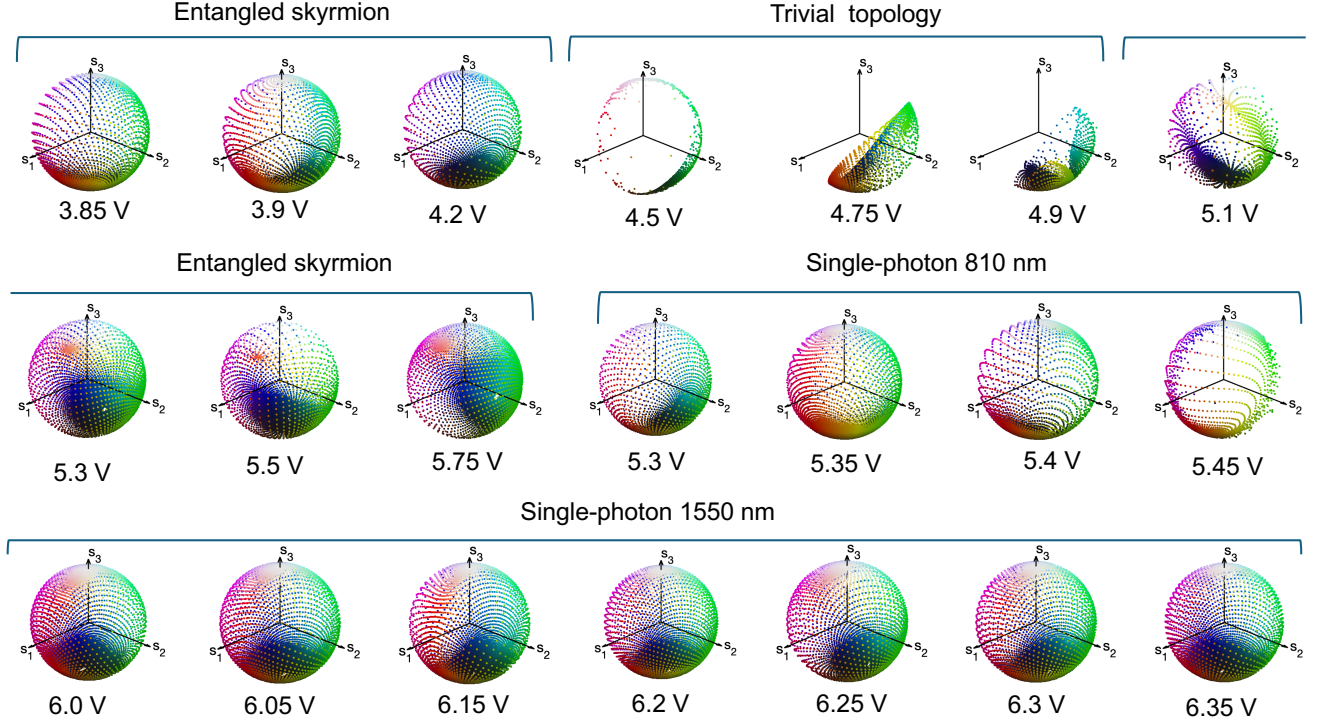


FIG. 7. Poincaré sphere representations of the polarization field $\mathbf{S}(x, y)$ at various applied voltages. Each sphere shows the spatially sampled Stokes vectors extracted from the reconstructed density matrices and projected onto the Poincaré sphere. The voltage sweep spans the different quantum topological regimes extracted in the experiment: entangled skyrmion (top rows), single-photon skyrmion at 810 nm and 1550 nm (middle and bottom rows), and the trivial topology region (centered around 4.5–4.9 V). Dense and near-complete coverage of the sphere indicates robust topological structure ($N \approx -2$), while sparse or localized distributions correspond to trivial or partially degraded topology.

this form exhibits the same essential feature: the entire state exists as a coherent superposition of two distinct configurations with correlations between the subsystems.